Rapid prediction of real-time thermal characteristics, solidification parameters and microstructure in laser directed energy deposition (powder-fed additive manufacturing)

Yuze Huang[a], Mohammad Ansari[a], Hamed Asgari[a], Mohammad Hossein Farshidianfar[b], Dyuti Sarker[a], Mir Behrad Khamesee[b], Ehsan Toyserkani[a],[*]

[a] Multi-Scale Additive Manufacturing Lab, Department of Mechanical and Mechatronics Engineering, University of Waterloo, Waterloo, Ontario, N2L 3G1, Canada
[b] Department of Mechanical and Mechatronics Engineering, University of Waterloo, Waterloo, Ontario, N2L 3G1, Canada

ABSTRACT

The localized thermal characteristics, solidification parameters and the corresponding microstructure depend highly on the process parameters in the laser powder-fed additive manufacturing (LPF-AM) process. However, undesirable and inconsistent microstructure may potentially be induced due to the environmental disturbances or improper setting of process parameters. This research correlates the process parameters to the localized transient thermal characteristics, i.e. temperature and cooling rate, and solidification parameters, namely thermal gradient (G) and solidification rate (R) for rapid prediction of the microstructural evolution. The built correlation can also be used for parameter optimization and could be potentially employed for in-situ microstructural control. Firstly, the thermal characteristics and the solidification parameters were resolved from a three-dimensional analytical thermal model that couples the powder mass flow and the laser heat flux. Subsequently, the calculated solidification parameters were combined with the substructure scale solutions for microstructure prediction with respect to the solidification map. In the end, experiments of LPF-AM were conducted with stainless steel 316L (SS 316L) and Inconel 625 powders to validate the built correlation. It was noticed that the calculated real-time melt pool peak temperatures match well with the experimental results at different laser scanning speeds and diverse energy densities in the SS 316L deposition. The predicted microstructural evolutions show reasonable agreement with the experimental observations for both SS 316L and Inconel 625 depositions under different scanning speeds. In addition, it was found that the combination of a higher scanning speed with a lower laser power results in a finer microstructure, but the combinations should be kept within the melt pool temperature thresholds for effective deposition. Moreover, the $G \times R$ values increase from the bottom to the top of the melt pool bead, leading to a finer microstructure at the top zone for both SS 316L (5.5 μm average primary dendrite arm spacing) and Inconel 625 (3 μm average secondary dendrite arm spacing) deposits. On the contrary, the G/R values decrease from the bottom to the top of the melt pool bead, which in turn, give rise to the gradual transition of the substructure morphology from columnar dendritic to equiaxed dendritic for the Inconel 625 deposits.

1. Introduction

Laser powder-fed additive manufacturing (LPF-AM), a class of laser-based directed energy deposition, has been used for three-dimensional (3D) parts fabrication (Mazumder and Qi, 2005), surface coating (Feng et al., 2017), and worn out components repair (Vilar and Almeida, 2015). In the LPF-AM process, the metal powder is delivered through a carrier inert gas stream onto the substrate/object surface, which is melt immediately by the high-energy laser source and solidifies as the laser passes away. According to the predefined scanning pattern, further powder is deposited, melted and solidifies to form new features on the existing substrate/object in a layer-by-layer approach. The above complex procedures of LPF-AM involve a large variety of processing parameters, mainly including laser power, laser scanning speed, laser absorptivity, laser beam profile, powder feed rate, powder stream profile and carrier gas flow rate (Toyserkani et al., 2004b). These parameters are all sensitive to the environmental disturbances and influence each other (Hu and Kovacevic, 2003). Moreover, the LPF-AM process has a highly localized and dynamic thermal behavior. This may result in undesirable microstructural features and inconsistent

mechanical properties of the fabricated parts due to the change of local processing conditions (Wolff et al., 2017). All these variabilities and inconsistencies may degrade the performance of the LPF-made parts.

However, the characterization and validation of geometrical, microstructural and mechanical properties of as-built parts are driven primarily by offline post-processing analysis, which is time-consuming and expensive (Knapp et al., 2017). So far, a variety of process parameters have been linked to geometrical features through online/inline control strategies to improve dimensional accuracies (e.g., melt pool dimension (Wang, Li et al., 2016), clad height (Toyserkani and Khajepour, 2006) and clad geometry (Fathi et al., 2008)). However, it should be noted the strategies that solely arrive at a high geometrical accuracy might not be sufficient if microstructure and mechanical properties of the fabricated parts are not desirable.

A large number of research studies have shown that the microstructural and mechanical properties of the LPF-AM fabricated parts are mainly governed by the real-time thermal characteristics of melt pool and the corresponding solidification parameters (thermal gradient (G) and solidification rate (R)). Additionally, the in-situ thermal characteristics and the associated solidification parameters depend highly on the process parameters. Akbari and Kovacevic (2018) found that the smaller inter-layer dwell time can decrease the cooling rate ($G \times R$), leading to a coarser grain size and lower ultimate tensile strength. Farshidianfar et al. (2016) reported that the size of the solidification structure and the associated solidification mode can be defined by the in-situ cooling rate, which is affected by the laser scanning speed, laser power and powder feed rate. Wang, Palmer et al. (2016) demonstrated that a lower linear heat input (laser power/scanning speed) is corresponding to a smaller-size melt pool, larger thermal gradient and higher cooling rate, therefore, resulting in higher yield strength, larger ultimate tensile strength and higher ductility compared to those of higher linear heat input. Furthermore, in the recent review work of Sames et al. (2016) for metallic material additive manufacturing, it was stated that the control of microstructural and mechanical properties could be achieved through the manipulation of local solidification parameters. Moreover, Collins et al. (2016) summarized the recent microstructural control work in metallic additive manufacturing and highlighted the key interdependencies among the processing parameters, composition and the resulting microstructure. They reported that the spatial-temporal solidification parameters could be estimated from the localized thermal behavior, which can be further controlled by varying processing parameters. Therefore, linking the process parameters to the real-time thermal characteristics and solidification parameters is highly required for developing on-line process control systems to manufacture parts with expected microstructural features and reliable mechanical properties in the LPF-AM process.

Numerous research studies have been done to establish the correlation between thermal characteristics, solidification parameters, and process parameters for the microstructural and mechanical properties control and optimization. Lia et al. (2018) measured the real-time thermal cycles in the LPF-AM process and calculated the corresponding G, R and $G \times R$ to evaluate the microstructural evolution. They showed that the process variables could be associated with the solidification parameters that govern the final microstructure. Using fitted relationships of the cooling rate and the secondary dendritic arm spacing (SDAS, SDAS is a common length scale for cellular/dendritic microstructure), the size of the microstructure can be predicted. However, the directly measured thermal data can only be used to represent thermal characteristics of the specific local zone. It has been argued that LPF-AM is a highly localized solidification process, in which the thermal behavior of each discrete location could differ significantly from that of the other positions (Collins et al., 2016).

Numerical modeling of the spatial-temporal thermal behavior is a possible alternative to the direct experimental measurement. Gockel et al. (2014) proposed an integrated approach to control the microstructure in the single-track deposition, which was later extended to

thin-wall structure (Gockel et al., 2015). The solidification parameters were derived from the numerical thermal model through Finite Element Method (FEM). Subsequently, the microstructure was predicted using the solidification map of the specific material. Finally, the indirect microstructure control was achieved by relating the predicted microstructure to the derived melt pool dimensional map. Knapp et al. (2017) built a digital twin of a single-layer deposition in LPF-AM. The spatialized transient temperature, cooling rate, and solidification parameters were extracted from a numerical heat transfer and fluid flow model for a given set of process parameters. Accordingly, the SDAS and the hardness were predicted based on the analytical relationships. In addition, their experimental results showed that the SDAS in the LPF-AM process could be calculated by the well-known Kurz-Fisher (KF) model (Kurz and Fisher, 1981) with high accuracy. Nevertheless, the FEM-based numerical models are computationally expensive and cannot be directly used for online control.

Since the direct experimental measurement and the FEM-based numerical modeling both have their limitations for a rapid estimation and online control of the thermal characteristics and microstructure, the time-efficient analytical thermal model could be considered as a potential choice. Bontha et al. (2006) built thermal process maps to estimate the solidification microstructure based on both analytical and numerical thermal models in thin-wall structure deposition, which was also extended to bulky 3D structures (Bontha et al., 2009). Temperature-independent material properties were assumed in the analytical model, while the temperature-dependent properties and latent heat were considered in the numerical model. They found that the predicted solidification parameters from the FEM-based numerical solution and the quasi-steady-state analytical Rosenthal solution are in a reasonable agreement with each other for both the small-scale (LPF-AM) and large-scale (higher power) deposition processes. Liang et al. (2016) developed a theoretical primary dendrite arm spacing (PDAS) model in terms of the process parameters and extended that to process-microstructure maps for microstructure control (Liang et al., 2017). In their study, the solidification parameters were numerically solved from the analytical quasi-steady-state Rosenthal equation. The calculated G and R were then related to the microstructural characteristics and were verified by the experimental results. However, the above quasi-steady-state Rosenthal solution only shows the thermal characteristics at the time $t \to \infty$, which may not be accurate to represent the time-varying thermal characteristics in the LPF-AM process. Consequently, these models may not be applicable for real-time microstructural control.

This research aims to link the process parameters to the transient localized thermal characteristics and solidification parameters for rapid prediction of the solidification microstructure induced during the LPF-AM process. The real-time thermal characteristics and the solidification parameters are extracted from a 3D analytical thermal model based on the process parameters. Subsequently, the calculated solidification parameters are combined with the substructure scale solutions for microstructural prediction. The structure scale solutions are handled by fitting the predicted solidification parameters with the measured PDAS and SDAS based on the well-known KF model (Kurz and Fisher, 1981). Validation experiments are conducted by depositing stainless steel 316 L (SS 316 L) and Inconel 625 at different laser scanning speeds. The predicted real-time melt pool peak temperatures at different scanning speeds and various energy densities of SS 316 L deposition are compared with the corresponding experimental results presented in the previous work (Farshidianfar et al., 2016). The variations in the solidification scale and mode over the SS 316 L and Inconel 625 deposits are also analyzed.

2. Mathematical model

The transient temperature field solution at the interest point $X = (x, y, z)$ of a moving 2D Gaussian laser heat source (TEM$_{00}$) with a powder feeding rate $\dot{m}$ in the lateral LPF-AM process (illustrated in
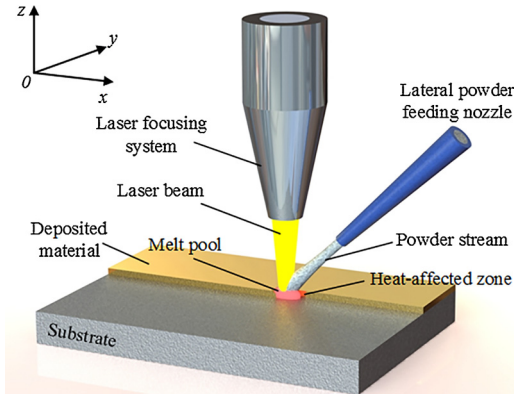
Fig. 1. Schematic of the lateral LPF-AM deposition process.

Fig. 1) is given by Huang et al. (2018)

$$T(X, t) = \frac{2}{\rho_P c_P \pi \sqrt{\pi \alpha_P}} \int_{\tau=0}^{\tau=t} d\tau \{ \frac{\beta_w P_L / \sqrt{(t-\tau)}}{R_L^2 + 8\alpha_P(t-\tau)} exp[-\frac{2[(x-v\tau)^2 + y^2]}{R_L^2 + 8\alpha_P(t-\tau)}$$
$$-\frac{z^2}{4\alpha_P(t-\tau)}] + \frac{c_P \dot{m}(T_0 - T_m)/\sqrt{(t-\tau)}}{[r_{avg}^2 + 8\alpha_P(t-\tau)]} exp[$$
$$-\frac{2[[(x-v\tau)/sin\varphi]^2 + y^2]}{r_{avg}^2 + 8\alpha_P(t-\tau)} - \frac{z^2}{4\alpha_P(t-\tau)}]\} + T_0 \quad (1)$$

Where, ρ_P is the density, c_P the specific heat, α_P the thermal diffusivity, β_w the process laser absorptivity, φ the nozzle angle, r_{avg} the average powder stream radius, T_0 the ambient temperature and eventually T_m is the melting temperature. The laser is turned on at time $\tau = 0$ with laser power P_L, laser radius R_L and moves along the *x*-axis with speed v. In the built coordinate, x, y and z represent the scanning direction, transverse direction and the deposit height direction, respectively. The derivation of the above solution is elaborated in Huang et al. (2018), which is developed based on Green's function with the absence of radiative and convective heat losses and had been verified by the single-track and multi-layers multi-tracks experiments.

It is well known that the linearly polarized laser beam absorption of an inclined plane is affected by its inclination angle (Brewster effect (Picasso et al., 1994)). For the circularly polarized laser beam in our case, the dynamic process laser absorptivity β_w may be expressed as (Steen and Mazumder, 2010),

$$\beta_w = \beta[1 + a_w tan^{-1}(h/D_L)] \quad (2)$$

Where, β is the absorptivity of the powder material for a flat surface, a_w the Brewster coefficient, h the deposit height and eventually D_L is the laser beam diameter. The dynamic deposit height is calculated based on the feeding powder mass balance as referred in Huang et al. (2018).

Experimental study from Lampa et al. (1997) showed that the value of thermal conductivity is at least twice larger than the stationary melt conductivity in the presence of thermocapillary flow (Marangoni flow). In this research, the thermocapillary flow is compensated by adding a correction factor μ_M to the initial thermal conductivity as (Toyserkani et al., 2004a),

$$k^*(T) = \mu_M k(T_m), \ T > T_m \quad (3)$$

Where, $k^*(T)$ is the modified thermal conductivity at temperature T.

The latent heat of fusion in melting/solidification cycles is not considered since it is much smaller than the energy amount required for melting the metallic powder (Rubenchik et al., 2018). Consequently, the influence of ignoring the latent heat of fusion on the thermal characteristics calculation is expected to be insignificant as stated by Yang et al., 2018. The effects of radiation, convection and evaporation are also not included in this research. Previous studies from (Gedda et al., 2002; Pinkerton and Li, 2004) suggested that the heat loss by
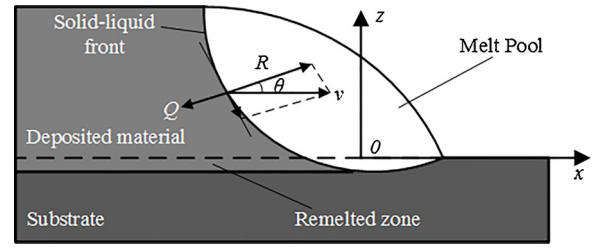
Fig. 2. Schematic diagram of the solidification front in the longitudinal centerline cross-section (y = 0) of the single-track deposition. Laser scanning speed v, solidification rate R and local predominant heat flow Q.

these effects is negligible compared to the dissipation of heat by conduction in the LPF-AM process.

After solving the transient thermal field based on Eqs. (1–3), the cooling rate $\dot{T}$ for any interest point $X = (x, y, z)$ may be derived as,

$$\dot{T} = \partial T(X,t)/\partial t \quad (4)$$

The temperature gradient G on the solidification front can also be derived from the temperature field solution as,

$$G = \sqrt{\left[\frac{\partial T(X,t)}{\partial x}\right]^2 + \left[\frac{\partial T(X,t)}{\partial y}\right]^2 + \left[\frac{\partial T(X,t)}{\partial z}\right]^2} \quad (5)$$

In the LPF-AM process, the laser beam moves continuously and the solidification front keeps pace with the advancing laser source as shown in Fig. 2. As the local solidification front moves along the maximum temperature gradient, which is normal to the solid-liquid front and opposite to the local predominant heat flow direction Q, the solidification rate R may be calculated by (Zheng et al., 2008),

$$R = v cos\theta \quad (6)$$

Where, θ is the angel that between the local solid-liquid front normal and the laser scanning direction. Since θ is nearly $90\mathring{0}$ at the bottom part of the melt pool and approach $\mathring{0}$ at the top region, the solidification rate will reach the minimum at the bottom region and approach the maximum at the top part.

The angle θ may be derived based on the thermal solution in the longitudinal centerline cross-section as (Wei et al., 2015),

$$cos\theta = \frac{\partial T(X,t)/\partial x}{\sqrt{[\partial T(X,t)/\partial x]^2 + [\partial T(X,t)/\partial z]^2}} \quad (7)$$

It has to be noted that there is no temperature gradient in the transverse direction ($\partial T(X,t)/\partial y$) at the longitudinal centerline cross-section. From Eqs. (6 and 7), the solidification rate in the longitudinal centerline cross-section may be derived as,

$$R = \frac{\partial T(X,t)/\partial t}{\sqrt{[\partial T(X,t)/\partial x]^2 + [\partial T(X,t)/\partial z]^2}} \quad (8)$$

Similarly, for the spatial point $X = (x, y, z)$ in the Cartesian coordinate system, $cos\theta$ can be directly calculated as $cos\theta = [\partial T(X,t)/\partial x]/\sqrt{[\partial T(X,t)/\partial x]^2 + [\partial T(X,t)/\partial z]^2 + [\partial T(X,t)/\partial z]^2}$ and the corresponding solidification rate can be expressed as $R = \dot{T}/G$.

The dendrite arm spacing (DAS) λ has been established based on the solidification parameters (G and R) by the well-tested Kurz and Fishers' model (Kurz and Fisher, 1981),

$$\lambda = AG^{-n}R^{-m} \quad (9)$$

where, A, n, and m are material-dependent parameters. The DAS provides a useful approach to establish the precise effect of solidification conditions on microstructure. Especially, the SDAS can be calculated by setting $n = m$ based on Eq. (9).
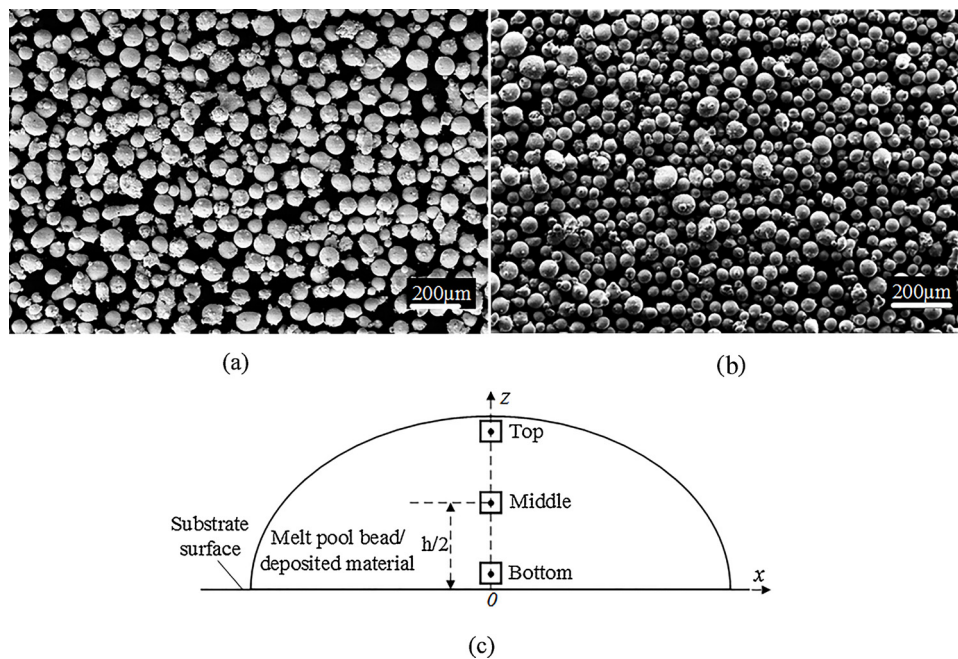
Fig. 3. SEM images of the powder particles (a) SS 316 L, (b) Inconel 625 and (c) schematic diagram showing the three different locations in the transverse cross-section of the bead/deposit for solidification parameter prediction and microstructure verification.

3. Materials and procedure

In this research, SS 316 L powder (Praxair Surface Technologies, PA, USA), -325 mesh, was deposited on the sandblasted AISI 1030 medium carbon steel substrate by an in-house developed LPF-AM apparatus. With the same apparatus, Inconel 625 powder (Carpenter, Pennsylvania, USA) in the size range of 45–125 μm was deposited on the sandblasted Inconel 625 plates. The LPF-AM apparatus was composed by a continuous 1.1 kW IPG photonics fiber laser system, a Sulzer Metco powder feeder and a Fadal CNC machine. The morphology of powder particles was studied using a Zeiss LEO FE-SEM 1530 scanning electron microscope (SEM). SEM images of the powder particles (SS 316 L and Inconel 625) are shown in Fig. 3. As seen, in both powders (Fig. 3(a) and (b)), most of the particles possess a spherical morphology while a few powder particles with other morphologies, e.g. irregular or satellite-like, can also be identified. The thermo-physical properties of the SS 316 L and Inconel 625 powders are assumed to be temperature independent and the associated thermal parameters (shown in Table 1) were averaged over the temperature range. The fiber laser absorptivity was chosen as 0.4 (Wen and Shin, 2010) and 0.35 (Ahmed et al., 2010) for SS 316 L and Inconel 625, respectively.

Experiments were done to test the developed relations with single-layer deposition. The process parameters used in the present research are listed in Table 2. To study the microstructural features using optical and scanning electron microscopy, the samples were cross-sectioned at the middle track length, mounted and polished using conventional metallography methods, followed by etching. The SS 316 L and the Inconel 625 samples were etched by Marble's reagent (10 g $CuSO_4$ in 50 mL HCl and 50 mL H_2O) and Glyceregia reagent (10 mL glycerol, 50 mL HCl and 10 mL HNO_3), respectively. The DAS was measured in

Table 2
Process parameters for SS 316 L and Inconel 625 depositions.

Process parameters	SS 316 L	Inconel 625
Scanning speed, [mm/min]	25, 50, 100, 200	180, 270, 360
Laser power, [W]	700, 917	1000
Powder feed rate [g/min]	4	7
Laser beam diameter, [mm]	2.5	1.8
Nozzle angle,	5$\overset{\circ}{5}$	6$\overset{\circ}{0}$
Nozzle height, [mm]	10	7
Correction factor, μ_M	2.5	2.5
Ambient temperature, [K]	300	300
Brewster effect coefficient, a_w	0.0196	0.0196
Laser absorptivity	0.4	0.35
Carrying gas feed rate, [dL/min]	3.5	2.5
Track length, [mm]	30	30
Powder stream divergence angle	8.3	8.4

three different height locations of the deposits as illustrated in Fig. 3(c): the bottom region that is close to the fusion boundary (around $1/8\,h$); the middle region that is equidistant from the bottom and top edges ($1/2\,h$); and the top region located at around the deposit top (around $7/8\,h$). The DAS of the SS 316 L deposits were measured based on the Hilliard single-circle procedure followed by the ASTM standard (Standard, 2004), while the DAS of the Inconel 625 deposit were measured individually by the Digimizer@ software with hundreds of measurements and then averaged. The melt pool real-time temperature data of SS 316 L deposition were used from the previous work (Farshidianfar et al., 2016). The calculation of the real-time thermal and solidification characteristics were conducted in the Matlab® R2017b by a HP® computer with Intel® Core™ i7-6700 CPU (3.4 GHz).

Table 1
Particle thermal-physical properties. The SS 316 L thermal-physical properties were obtained from references (Khairallah and Anderson, 2014; Roy et al., 2018). Inconel 625 properties were obtained from reference (Arısoy et al., 2019).

	Solidus T_s, Liquidus T_l and Melting T_m temperature [K]	Density ρ_P [Kg/m^3]	Thermal conductivity k [$W/(m \cdot K)$]	Specific heat c_P [$J/(Kg \cdot K)$]
SS 316 L	1680, 1720,1700	7900 (300 K)–7430 (1700 K)	13.96 (300 K)–35.95 (1700 K)	434 (300 K)–965 (1700 K)
Inconel 625	1563,1623, 1593	8440	9.8 (300 K)–25.6 (1273 K)	410 (300 K)–670 (1363 K)
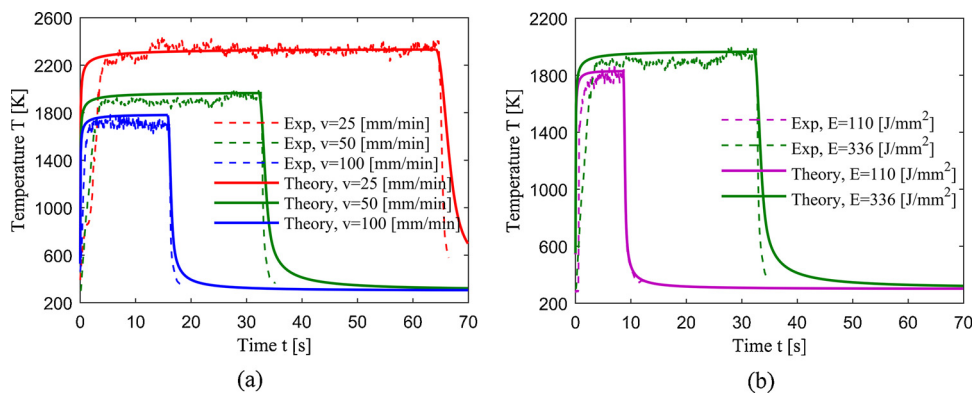
Fig. 4. Real-time melt pool top surface peak temperature of SS 316 L deposition under following conditions. (a) Different laser scanning speeds (laser power 700 W) and (b) different energy densities (E = 110 J/mm^2 with laser power 917 W, scanning speed 200 mm/min; E = 336 J/mm^2 with laser power 700 W, scanning speed 50 mm/min). Powder feed rate 4 g/min. The real-time melt pool peak temperature was adopted from a previous work (Farshidianfar et al., 2016).

4. Results and discussion

4.1. Real-time temperature evolution

Fig. 4 shows that the model predicted results, calculated based on Eqs. (1–3), are in a good agreement with the experimental measurements of the real-time melt pool peak temperature under different laser scanning speeds and various energy densities (P_L/vD). As seen in Fig. 4(a), the melt pool peak temperature decreases significantly with an increase in the laser scanning speed. This is because the energy density declines with the increase in the scanning speed, leading to a smaller amount of laser energy were added into the melt pool at per unit time. To further verify the effect of energy density on the peak temperature, the laser power and scanning speed were varied simultaneously to obtain the two different energy densities as shown in Fig. 4(b). As seen, a higher peak temperature is achieved with a larger energy density. Slight mismatches are also observed between the measured data and the model predictions, which may be ascribed to error/noise sources in the temperature measurement during deposition as well as the simplifying assumptions made for the thermal model.

The agreement between the calculated real-time melt pool peak temperature and the corresponding experimental measurements may provide sufficient confidence in using the thermal model to link the process parameters to the in-situ thermal characteristics. According to the mathematical model described in Section 2, the melt pool peak temperature map was plotted as a function of laser power and scanning speed as shown in Fig. 5. As seen, the maximum temperature occurs at the largest laser power and minimum scanning speed. However, the peak temperature has to be chosen in a way that the maximum temperature is higher than the melting temperature (1700 K) but lower
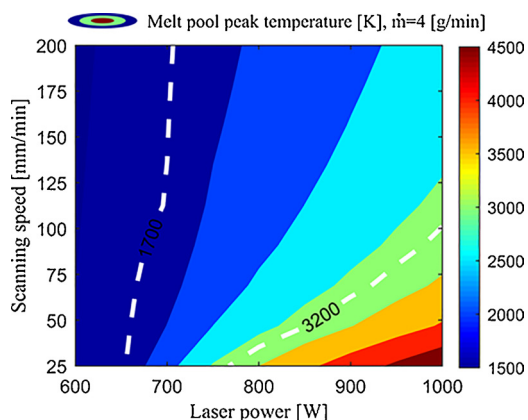
than the boiling temperature (3200 K (Gusarov et al., 2009)) in the process window for effective deposition. The developed melt pool peak temperature map illustrated in Fig. 5 can be effectively useful to optimize the process parameters to achieve an effective deposition.

In LPF-AM, each location on the scanning route experiences a dynamic thermal cycle because the temperature rises up as the laser beam gets closer and then cools down when the laser passes away. In addition, the energy of the laser beam typically has a non-uniform distribution (e.g., Gaussian distribution), giving rise to an inconsistent temperature distribution within the melt pool. Therefore, the measured real-time top surface temperature of the melt pool shown in Fig. 4 may not be accurate enough to estimate the local thermal characteristics of different zones within the melt pool area, particularly for the zones beneath the melt pool surface.

According to the thermal model described in Section 2, the local thermal history of the SS 316 L deposition at different depth locations (Fig. 3(c)) of the melt pool bead are calculated and shown in Fig. 6. Fig. 6(a) shows the local thermal cycles in the single-layer deposition. It is observed that both top and bottom locations will experience a thermal cycle with the motion of the laser beam along the track path. In this situation, the temperature of the top and bottom locations increases instantly from the low ambient value to a high magnitude (e.g., T_s, T_l) and then decreases over time. It is evident from Fig. 6 that a higher cooling rate and a larger peak temperature can be reached at the top location than that of the bottom location at the same scanning speed. This is in a good agreement with both the experimental result reported by Du et al. (2018) and the numerical simulation founding from Gan et al. (2017). Moreover, the instantaneous heating/cooling rates (Fig. 6(b)) are inversely proportional to the scanning speed for both bottom and top locations of the melt pool bead.

4.2. Solidification characteristics

Temperature gradient (G) and solidification rate (R) are the two main parameters affecting the solidification microstructure. The effect may be illustrated by the solidification map as presented in Fig. 7. The solidification map is constructed by G and R in the combination forms with $G \times R$ (cooling rate) and G/R, where the G/R ratio governs the solidification mode while their product ($G \times R$) controls the scale of the solidification microstructure (Kurz et al., 1986). As seen in Fig. 7, the solidification mode may transform from planar to cellular, columnar dendritic and equiaxed dendritic as the G/R ratio decreases. Additionally, a higher value of $G \times R$ will induce a finer substructure and consequently, may improve the mechanical properties of the fabricated parts (e.g., the yield stress (Hansen, 2004)).

Previous papers (Bontha et al., 2009, 2006; Cao et al., 2017) have shown that G, R and their associated combinations, i.e. $G \times R$ and G/R, vary significantly throughout the melt pool bead depth. As a result, the microstructure may be graded over the deposit height. However, measuring the G and R over the melt pool bead depth during the

Fig. 5. Melt pool peak temperature map for SS 316 L single-track deposition. The peak temperature was calculated at the transient time moment ($t = L/2v$, track length $L = 30$ mm). The melting temperature (1700 K) and boiling temperature (3200 K) of SS 316 L are marked with white dash lines.
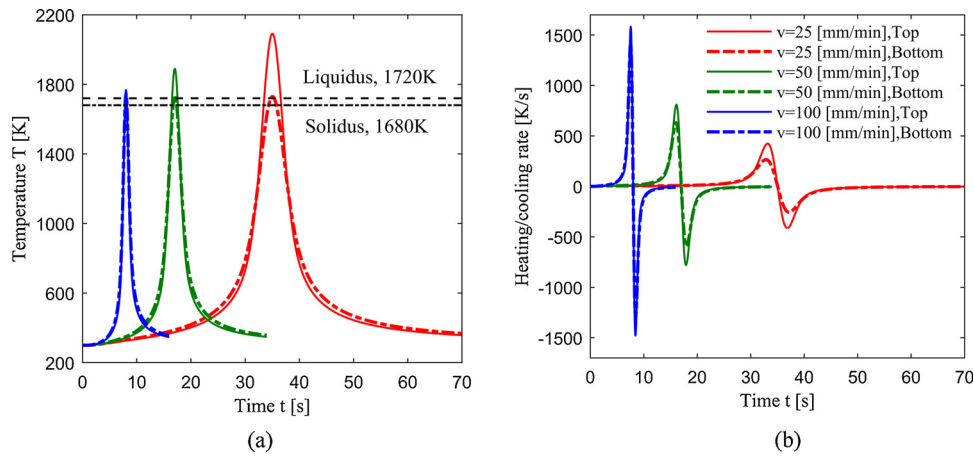
Fig. 6. Real-time local thermal profiles at different clad height locations during single-layer SS 316 L deposition. (a) Temperature cycles. (b) Heating/cooling rate. Laser power 700 W, powder feed rate 4 g/min. The liquidus and solidus temperatures of SS 316 L are marked with black dash lines.
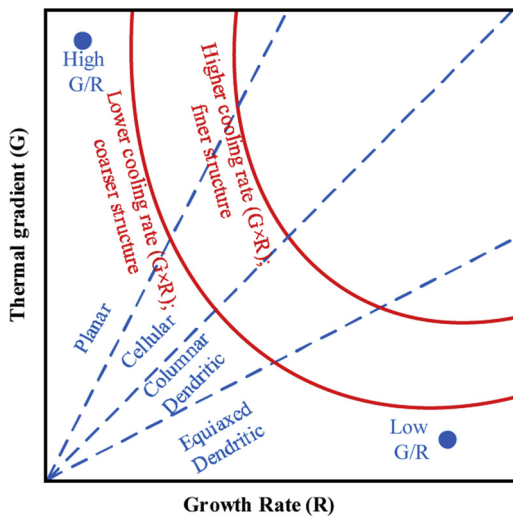
Fig. 7. Effect of G and R on the mode and scale of solidification microstructure. Adopted from reference (Kou, 2002).

process remains extremely challenging due to the small-scale localized melting nature and the high solidification rate. With the mathematical model developed in Section 2, the G and R can be calculated based on the Eqs. (5–8). Then a comparison of simulated $G \times R$ and G/R is performed for different locations along the melt pool bead depth, respectively. The transient cooling rate and the thermal gradient of the solidification front are both calculated at the time moment ($t = t_{T_s}$) of the last solidus temperature.

The calculated results of $G \times R$ and G/R for different depth locations of SS 316 L and Inconel 625 melt pool beads are shown in Fig. 8(a–d), respectively. Here has to be noticed that the three melt pool bead depth locations corresponding to the three deposit height locations as illustrated in Fig. 3(c). As seen from Fig. 8, with keeping all parameters constant but increasing the scanning speed, the cooling rates ($G \times R$) increase significantly for all three locations, while G/R ratios decrease. Moreover, the cooling rate ($G \times R$) increases from the bottom toward the top of the melt pool bead. By contrast, the G/R value decreases from the bottom location to the top region. The above simulated results are consistent with the previously reported experimental results, in which cooling rate ($G \times R$) decreases and G/R ratio increases with an increase in bead depth (Du et al., 2018; Gan et al., 2017) or with a decrease in scanning speed (Ou et al., 2018; Yin and Felicelli, 2010). The simulated cooling rates shown in Fig. 8 are in the range of $10^2 \sim 10^3$ K /s for both SS 316 L and Inconel 625 depositions.

Other studies have also reported that the cooling rates for SS 316 L (Hofmeister et al., 2001; Tan et al., 2011) and Inconel 625 (Lia et al., 2018) depositions by LPF-AM are in the range of $10^2 \sim 10^4$ K /s.

The microstructure evolution in SS 316 L and Inconel 625 deposits may be directly estimated from the predicted solidification parameters (Fig. 8) with refer to the general solidification map (Fig. 7). According to the calculated solidification parameters shown in Fig. 8, it can be concluded that the microstructure gradually become finer from the bottom to the top of the deposits due to the variation of cooling rate ($G \times R$). Furthermore, from Fig. 8 it is seen that the calculated G/R ratios for SS 316 L and Inconel 625 deposits are in the range of $900 \sim 6000$ Ks /mm^2 and $500 \sim 1000$ Ks/mm^2, respectively. Kurz and Fisher (1998) defined the threshold for planar solidification as $G/R = \Delta T_l/D$, where $\Delta T_l = T_l - T_s$ is the solidification temperature interval and D is the diffusion coefficient within the liquid phase. In some previous research works, the $\Delta T_l/D$ values for SS 316 L and nickel-based alloys have been reported as 50000 Ks/mm^2 (Scipioni Bertoli et al., 2019) and 7000 Ks /mm^2 (Blecher et al., 2014), respectively. These values far exceed the predicted G/R values (shown in Fig. 8). Consequently, it can be concluded that planar solidification will not occur for both SS 316 L and Inconel 625 deposits. The predicted G/R value (shown in Fig. 8(b)) for SS 316 L are also larger than that of reported for equiaxed solidification ($G/R = 10$ Ks /mm^2 (Zhang et al., 2014)). Therefore, columnar or cellular structure may be observed in the SS 316 L deposits. In comparison to the columnar-to-equiaxed transition (CET) curve of Inconel 625 reported by Hu et al. (2018), the estimated G/R values (shown in Fig. 8(d)) for Inconel 625 fall in the specific G/R window of equiaxed and columnar dendritic substructure. Accordingly, transition from columnar dendritic to equiaxed dendritic may occur in the Inconel 625 deposits.

To validate the predicted solidification parameters, the transverse cross-section micrographs of the SS 316 L and Inconel 625 deposits were investigated in the bottom, middle and top regions (illustrated in Fig. 3(c)) of deposits and the results were shown in Figs. 9 and 10, respectively. Fig. 9 shows the microstructure of the SS 316 L deposits under various laser scanning speeds. As seen, all samples exhibit a typical cellular microstructure in the transverse cross-section, which agrees with the predictions presented in the above paragraph. In addition, the PDAS shrinks dramatically as the laser scanning speed increases. This may be attributed to the fact that a larger cooling rate ($G \times R$) will be induced by a higher scanning speed, resulting in a finer microstructure as illustrated in the solidification map (Fig. 7). In addition, it is noticed that a coarser cellular structure is prevalent at the bottom zone of the deposit and the PDAS decreases towards the top zone (shown in Fig. 9). This kind of trend has also been found in the studies conducted by Yadroitsev et al. (2013) with SS 316 L powder and
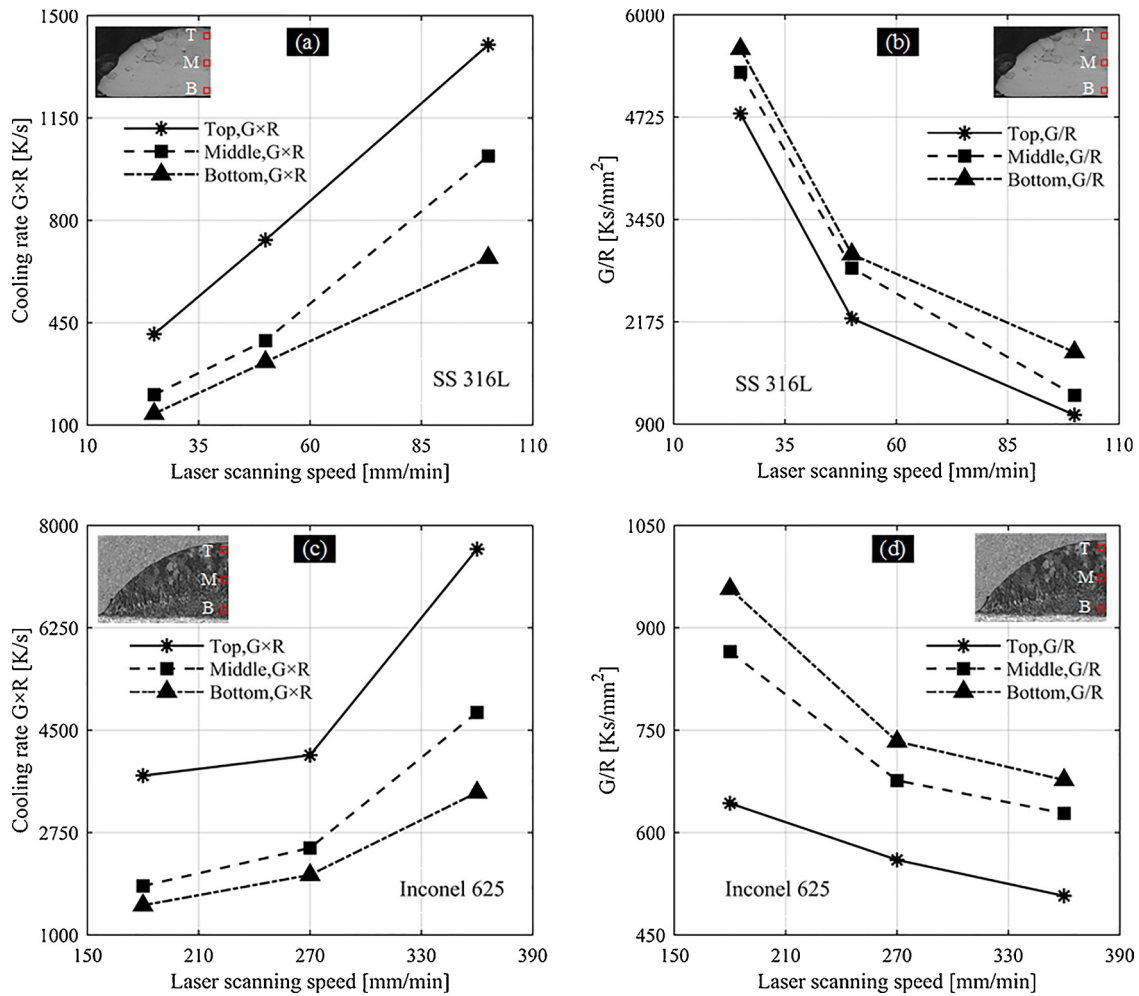
Fig. 8. Predicted in-situ solidification characteristics at different melt pool bead depth locations versus the laser scanning speed for the transient time moment $t = L/2v$. (a) (c) and (b) (d) are the cooling rate G × R and G/R ratio for SS 316 L and Inconel 625, respectively. 700 W laser power and 4 g/min powder feed rate were used for SS 316 L simulation, and 1000 W laser power and 7 g/min powder feed rate were used for Inconel 625 simulation. Track length $L = 30$ mm. The three different height locations in the final deposit were marked with red blocks to represent the corresponding depth locations in the melt pool bead. T, M and B represents the top, middle and bottom positions, respectively. (For interpretation of the references to colour in this figure legend, the reader is referred to the web version of this article).

Gan et al. (2017) with Co-based alloy powder. The above-observed microstructural variations (Fig. 9) are consistent with the calculated solidification parameters (Fig. 8) and the associated predicted microstructural evolutions that were discussed in the above paragraph.

Fig. 10 shows the microstructure of the Inconel 625 deposits in the transverse cross-section under different laser scanning speeds. Fig. 10(a) presents the microstructure profiles of the entire deposit at low magnification and Fig. 10(b) displays the microstructure profiles along the centerline of the deposit height at high magnification. It is evident that, for the regions with increasing distance to the substrate surface (from the bottom to the top regions of the deposits), different microstructures show up with decreasing size. Columnar-dendritic substructure without secondary dendrites is predominantly distributed near the bottom zones of the deposits. These relatively large columnar dendrites (PDAS of 8 ~ 12 μm) are observed in all the samples under the three different scanning speeds (180, 270, 360 mm/min). Columnar-dendritic substructure with classical secondary dendrites (SDAS of 3.6 ~ 5 μm) were observed in the middle region of the deposit. In addition, the transition of substructure from columnar dendrite to finer equiaxed dendrite (SDAS of 3 ~ 4μm) is noticed at the top region. Similar solidification microstructure evolution was also observed in the research work done by Xu et al. (2017) for Inconel 625 deposition by LPF-AM.

The microstructural evolution presented in Fig. 10 is consistent with

the above microstructure predictions that are derived from the calculated solidification parameters (shown in Fig. 8). At the melt pool bead bottom region, the solidification rate ($R = v\cos\theta$) is quite small since the normal of the local solidification front is nearly perpendicular to the laser travelling direction ($\theta \approx 90°$), resulting in a relatively large G/R value as shown in Fig. 8(d). Therefore, the typical columnar dendrites formed and no secondary dendrites grew near the bottom region. With an increase in distance from the substrate surface, the G/R value decreases (shown in Fig. 8d) due to the rapid growing solidification rate. This results in the gradual transition of the solidification mode from columnar dendritic to equiaxed dendritic. Meanwhile, the solidification front becomes less stable at a reduced G/R ratio, which in turn, promotes the growth of the secondary dendrites. Furthermore, the substructure scale decreased with an increase in the scanning speed as well as an increase in distance from the substrate surface, which is attributed to the highly increased cooling rate ($G × R$) as depicted in Fig. 8(c).

To quantitatively analyze the scale of solidification microstructure in the LPF-AM process, the DAS values were measured for different height locations of the deposits (illustrated in Fig. 3(c)) under various scanning speeds, where the results are presented in Fig. 11. Considering the fact that the secondary dendrites are not prominent in all regions of the SS 316 L deposits (Fig. 9), the PDAS is used to represent the microstructure length scale. From Fig. 11(a), it can be clearly seen that the PDAS of the SS 316 L shrinks from approximately 16 μm to 5.5 μm
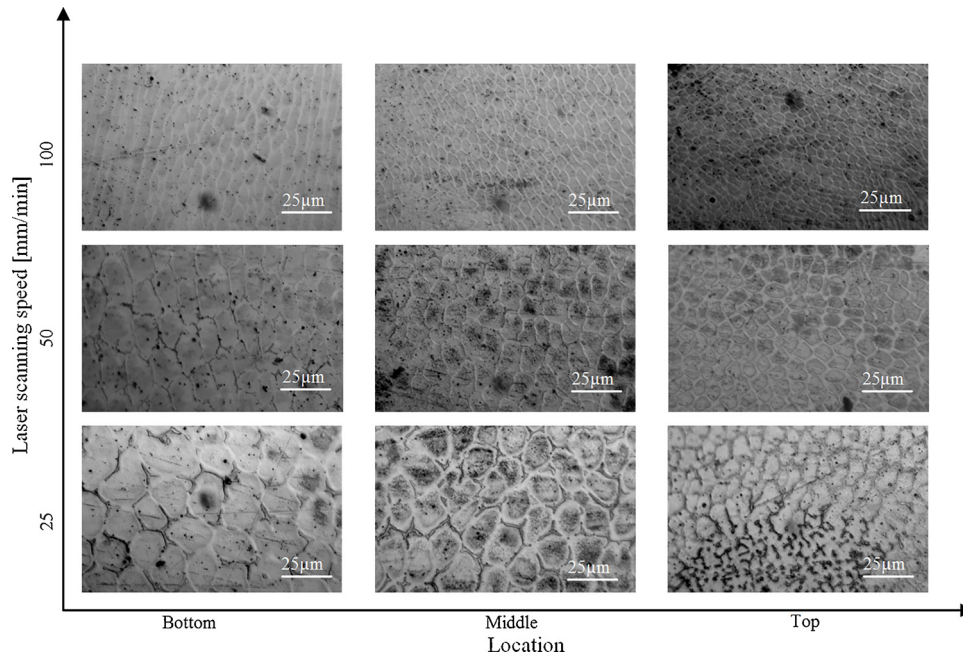
Fig. 9. High magnification images of the SS 316 L samples at different height locations of the deposits in the half-track length cross-section under different scanning speeds. Laser power 700 W, powder feed rate 4 g/min and track length 30 mm.
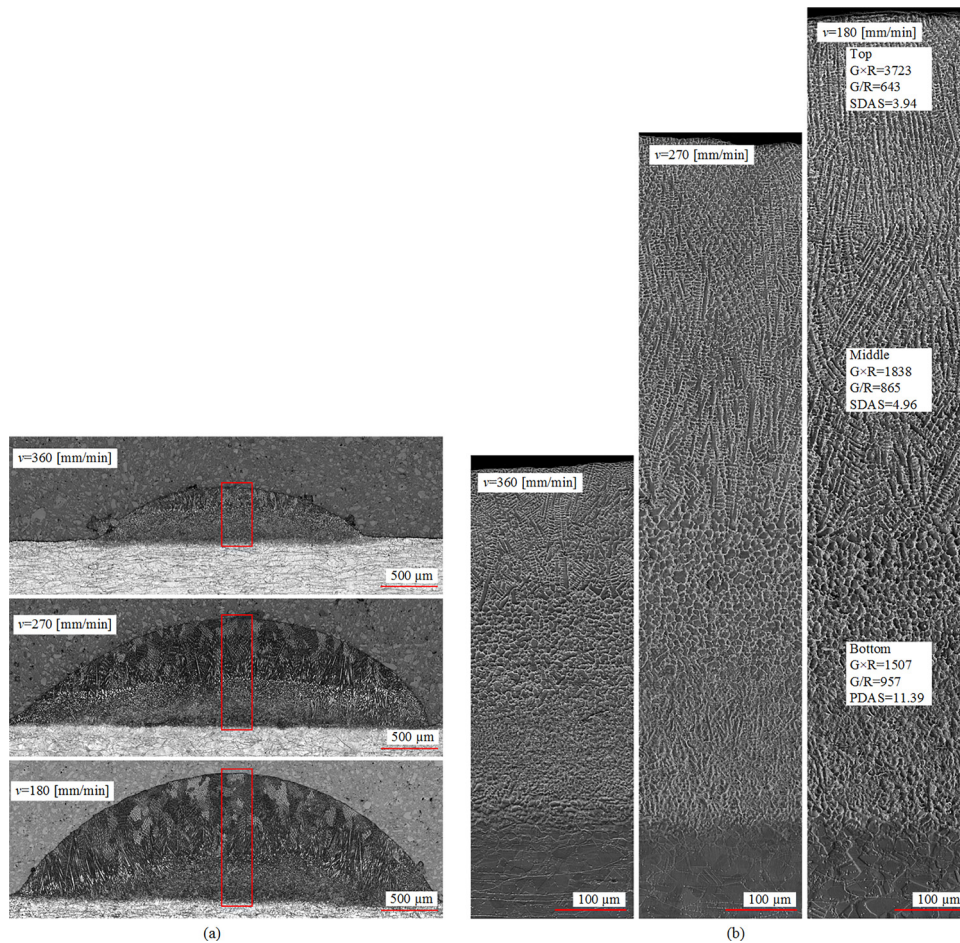
Fig. 10. SEM images of Inconel 625 samples in the half-track length cross-section at different scanning speeds. (a) Low magnification view (b) High magnification view along the clad height for the marked out area in (a) by red rectangles. The calculated $G \times R$ (K/s), G/R (Ks/mm^2) and the measured DAS (μm) for 180 mm/min scanning speed deposition were labeled in (b) for different height locations.
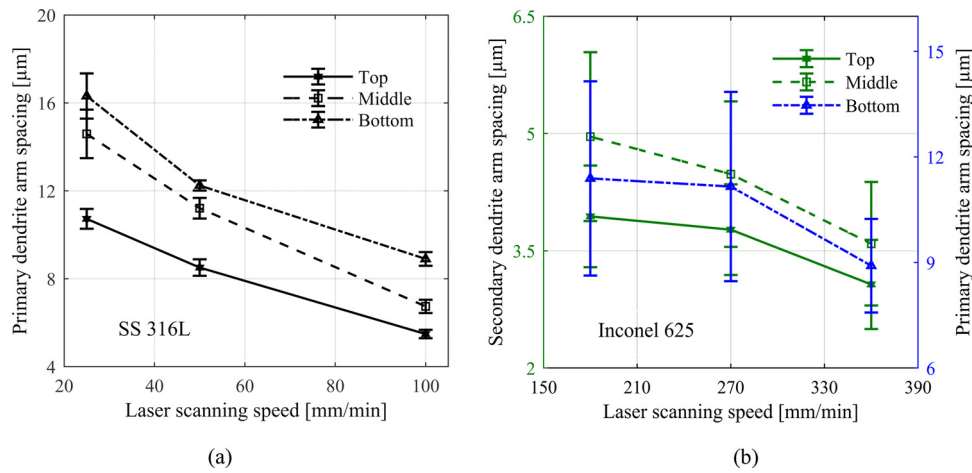
Fig. 11. Variation of the microstructure scale in dependence on the location and laser scanning speed. (a) PDAS for top, middle and bottom locations of the SS 316 L deposit (b) SDAS for middle and top location of Inconel 625 deposit and PDAS for bottom location of Inconel 625 deposit.

throughout the deposit when the scanning speed increases. These results are in agreement with the experimental PDAS values (6~12 μm) measured by Tan et al. (2011) for the SS 316 L deposits. Fig. 11(b) shows that with an increase of scanning speed, the SDAS and PDAS of Inconel 625 decreases from 5 μm to 3 μm and 11 μm to 9 μm, respectively. Similar SDAS and PDAS results (SDAS 3.5 μm and PDAS 10 μm) were reported by Marchese et al. (2017) for Inconel 625 samples deposited by LPF-AM.

The measured PDAS and SDAS values were related to the calculated solidification parameters (G and R) based on the well-tested Kurz and Fishers' model (Eq. (9)). The material-dependent coefficients A, n, and m were determined by using the least squares fit procedure. For the SS 316 L powder material, the exponents were set as $n = m = 1/3$ based on the previous study (Manvatkar et al., 2011). Subsequently, the constant A can be determined as $A = 80.37$ with a coefficient of determination $r^2 = 0.94$. Similarly, The SDAS of the Inconel 625 can be fitted with the calculated $G \times R$ values by setting the exponents as $n = m = 1/3$, and the constant A was then finalized as $A = 60.64$ with $r^2 = 0.99$. For the PDAS prediction of Inconel 625, the exponent values $n = 1/2$ and $m = 1/4$ have been proved to be reasonably accurate for nickel-based superalloys in the laser additive manufacturing process (Liang et al., 2016; Whitesell et al., 2000). Therefore, the constant A was determined as $A = 428.44$ with $r^2 = 0.944$. The fitted microstructure scale solutions and the measured PDAS and SDAS average values are shown in Fig. 12.

According to the built microstructure scale relationships shown in Fig. 12, the microstructure scale of the in-situ LPF-AM deposition may be predicted and viewed with respect to the primary process

parameters. Fig. 13(a) and (b) show the derived PDAS and cooling rate ($G \times R$) contour mappings in dependence on the process parameters for the top zone of the SS 316 L bead, respectively. The PDAS values were calculated by combining the predicted solidification parameters with the fitted substructure scale solutions. As seen from Fig. 13(a), the PDAS gradually grows with an increase in laser power. This is related to the fact that the higher laser power lowers the cooling rate as presented in Fig. 13(b), resulting in a coarser microstructure. More interestingly, it is observed from Fig. 13(a) that the PDAS has a higher variation rate over scanning speed compared to that of laser power. This variation pattern of the PDAS is consistent with that of the calculated cooling rate as illustrated in Fig. 13(b). As seen from Fig. 13(b), the cooling rate is more sensitive to scanning speed in comparison to laser power, which is in agreement with the experimental observations reported by Muvvala et al. (2017). Moreover, it is noticed that the finer microstructure could be achieved at the process parameter combination of higher scanning speeds with lower laser powers, as shown in Fig. 13(a). However, the parameter combination should be kept within the temperature threshold window (shown in Fig. 5) of the melt pool for an effective deposition.

5. Conclusions

In this study, the real-time localized transient thermal characteristics (temperature, cooling rate) and solidification parameters (thermal gradient and solidification rate) were linked to the process parameters for rapid prediction of the solidification microstructure in the LPF-AM process. Single-layer tracks of SS 316 L and Inconel 625 were deposited
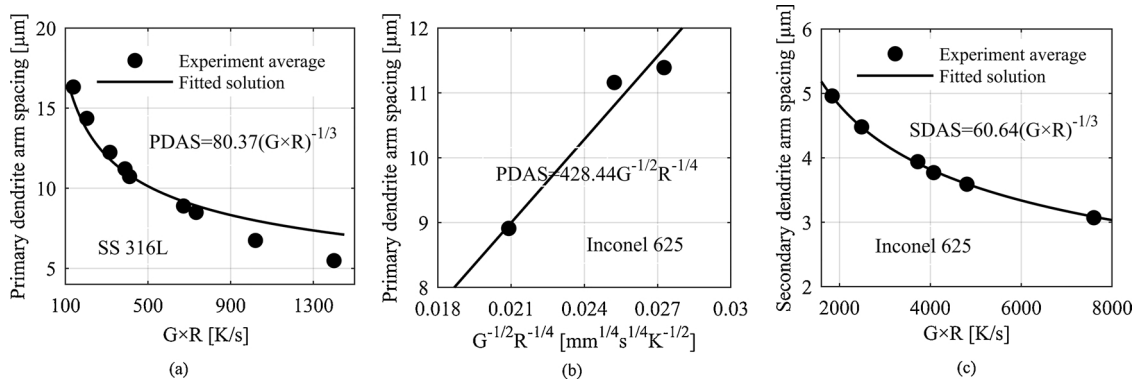
Fig. 12. Experiment measured PDAS (a), (b) and SDAS (c) averaged values and the fitted microstructure scale solutions in a function of thermal gradient and solidification rate.
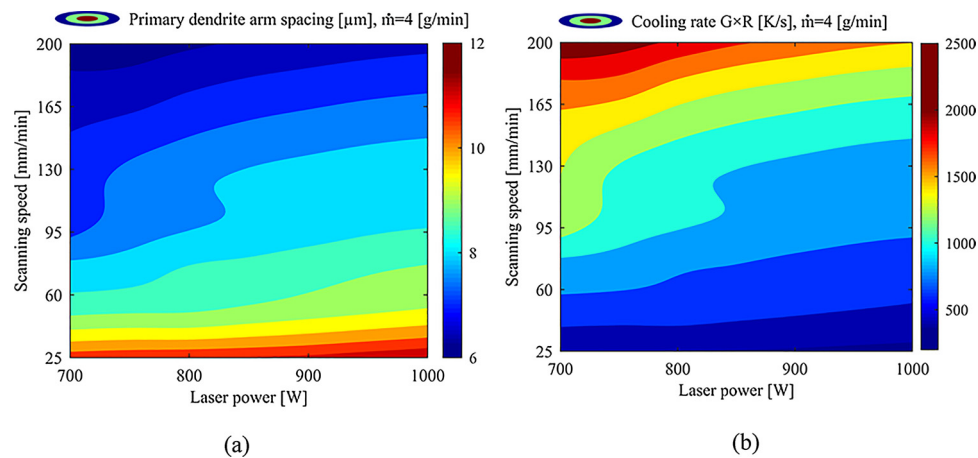
Fig. 13. PDAS map (a) and cooling rate map (b) in dependence on the laser power and scanning speed for the top zone of SS 316 L bead at the transient time moment (t = *L/2v*) with a cellular dendritic morphology.

at different laser scanning speeds to evaluate the above-mentioned relations. Based on the experimental and predicted results obtained in the present research, the following conclusions can be drawn:

(1)

(1) The calculated real-time peak temperatures of the melt pool are matched well with the corresponding experimental results of the previous research work (Farshidianfar et al., 2016) at different scanning speeds and various energy densities.

(2) The predicted microstructure variations are in a good agreement with the experimental observations of both SS 316 L and Inconel 625 deposits at different locations of the deposited tracks made at various scanning speeds.

(3) The DAS is more sensitive to scanning speed than laser power. Moreover, the finer microstructure could be achieved at the process parameter combination of higher scanning speed with lower laser power. However, to fulfill an effective deposition, the parameter combinations should be kept within the melt pool temperature threshold window.

(4) The cooling rate ($G \times R$) increases from the bottom to the top location of the deposits, leading to the finer microstructure at the top zone for both the SS 316 L and Inconel deposits. On the contrary, the G/R value decreases from the bottom location to the top location of the deposit, resulting in the gradual transition of the solidification mode for Inconel 625 deposits.

(5) The calculation time for the cooling rate ($G \times R$) and G/R ratio are around 40 ms with a tolerance of 10^{-3} in this study, confirming the potential of this work to be used for in-situ prediction of thermal and solidification characteristics as well as the real-time microstructural control. It should be mentioned that the calculation time might be considerably reduced with more advanced code optimization algorithms (e.g., switching from Matlab to a compiled programming language such as C++).

Acknowledgements

References

Ahmed, N., Voisey, K.T., McCartney, D.G., 2010. Investigation into the effect of beam shape on melt pool characteristics using analytical modelling. Opt. Lasers Eng. 48, 548–554. https://doi.org/10.1016/J.OPTLASENG.2009.12.013.

Akbari, M., Kovacevic, R., 2018. An investigation on mechanical and microstructural properties of 316LSi parts fabricated by a robotized laser/wire direct metal deposition system. Addit. Manuf. 23, 487–497. https://doi.org/10.1016/J.ADDMA.2018.08.031.

Arısoy, Y.M., Criales, L.E., Özel, T., 2019. Modeling and simulation of thermal field and solidification in laser powder bed fusion of nickel alloy IN625. Opt. Laser Technol. 109, 278–292. https://doi.org/10.1016/j.optlastec.2018.08.016.

Standard, Astm, 2004. E112-12:Standard Test Methods for Determining Average Grain Size. ASTM Int. 1–27. https://doi.org/10.1520/E0112-12.1.4. E112-12.

Blecher, J.J., Palmer, T.A., Debroy, T., 2014. Solidification map of a nickel-base alloy. Metallurgical and Materials Transactions A: Physical Metallurgy and Materials Science. Springer US, pp. 2142–2151. https://doi.org/10.1007/s11661-013-2149-1.

Bontha, S., Klingbeil, N.W., Kobryn, P.A., Fraser, H.L., 2009. Effects of process variables and size-scale on solidification microstructure in beam-based fabrication of bulky 3D structures. Mater. Sci. Eng. A 513–514, 311–318. https://doi.org/10.1016/J.MSEA.2009.02.019.

Bontha, S., Klingbeil, N.W., Kobryn, P.A., Fraser, H.L., 2006. Thermal process maps for predicting solidification microstructure in laser fabrication of thin-wall structures. J. Mater. Process. Technol. 178, 135–142. https://doi.org/10.1016/j.jmatprotec.2006.03.155.

Cao, S., Gu, D., Shi, Q., 2017. Relation of microstructure, microhardness and underlying thermodynamics in molten pools of laser melting deposition processed TiC/Inconel 625 composites. J. Alloys. Compd. 692, 758–769. https://doi.org/10.1016/j.jallcom.2016.09.098.

Collins, P.C., Brice, D.A., Samimi, P., Ghamarian, I., Fraser, H.L., 2016. Microstructural control of additively manufactured metallic materials. Annu. Rev. Mater. Res. 46, 63–91. https://doi.org/10.1146/annurev-matsci-070115-031816.

Du, L., Gu, D., Dai, D., Shi, Q., Ma, C., Xia, M., 2018. Relation of thermal behavior and microstructure evolution during multi-track laser melting deposition of Ni-based material. Opt. Laser Technol. 108, 207–217. https://doi.org/10.1016/J.OPTLASTEC.2018.06.042.

Farshidianfar, M.H.M., Khajepour, A., Gerlich, A.P.A.P., 2016. Effect of real-time cooling rate on microstructure in Laser additive manufacturing. J. Mater. Process. Technol. 231, 468–478. https://doi.org/10.1016/j.jmatprotec.2016.01.017.

Fathi, A., Khajepour, A., Durali, M., Toyserkani, E., 2008. Geometry control of the deposited layer in a nonplanar laser cladding process using a variable structure controller. J. Manuf. Sci. Eng. 130, 031003. https://doi.org/10.1115/1.2823085.

Feng, K., Chen, Y., Deng, P., Li, Y., Zhao, H., Lu, F., Li, R., Huang, J., Li, Z., 2017. Journal of materials processing technology improved high-temperature hardness and wear resistance of Inconel 625 coatings fabricated by laser cladding. J. Mater. Process. Tech. 243, 82–91. https://doi.org/10.1016/j.jmatprotec.2016.12.001.

Gan, Z., Yu, G., He, X., Li, S., 2017. Numerical simulation of thermal behavior and multicomponent mass transfer in direct laser deposition of Co-base alloy on steel. Int. J. Heat Mass Transf. 104, 28–38. https://doi.org/10.1016/j.ijheatmasstransfer.2016.08.049.

Gedda, H., Powell, J., Wahlström, G., Li, W.-B.B., Engström, H., Magnusson, C., Wahlstrom, G., Li, W.-B.B., Engstrom, H., Magnusson, C., 2002. Energy redistribution during CO2 laser cladding. J. Laser Appl. 14, 78–82. https://doi.org/10.2351/1.1471565.

Gockel, J., Beuth, J., Taminger, K., 2014. Integrated control of solidification microstructure and melt pool dimensions in electron beam wire feed additive manufacturing of ti-6al-4v. Addit. Manuf. 1, 119–126. https://doi.org/10.1016/j.addma.2014.09.004.

Gockel, J., Fox, J., Beuth, J., Hafley, R., 2015. Integrated melt pool and microstructure control for Ti–6Al–4V thin wall additive manufacturing. Mater. Sci. Technol. 31, 912–916. https://doi.org/10.1179/1743284714Y.0000000704.

Gusarov, A.V., Yadroitsev, I., Bertrand, P., Smurov, I., 2009. Model of radiation and heat transfer in Laser-Powder Interaction Zone at selective laser melting. J. Heat Transfer 131, 072101. https://doi.org/10.1115/1.3109245.

Hansen, N., 2004. Hall–Petch relation and boundary strengthening. Scr. Mater. 51, 801–806. https://doi.org/10.1016/J.SCRIPTAMAT.2004.06.002.

Hofmeister, W., Griffith, M., Ensz, M., Smugeresky, J., 2001. Solidification in direct metal deposition by LENS processing. JOM 53, 30–34. https://doi.org/10.1007/s11837-001-0066-z.

Hu, D., Kovacevic, R., 2003. Sensing, modeling and control for laser-based additive manufacturing. Int. J. Mach. Tools Manuf. 43, 51–60. https://doi.org/10.1016/S0890-6955(02)00163-3.

Hu, Y.L., Lin, X., Lu, X.F., Zhang, S.Y., Yang, H.O., Wei, L., Huang, W.D., 2018. Evolution of solidification microstructure and dynamic recrystallisation of Inconel 625 during laser solid forming process. J. Mater. Sci. 53, 15650–15666. https://doi.org/10.1007/s10853-018-2701-x.

Huang, Y., Khamesee, M.B.M.B., Toyserkani, E., 2018. A new physics-based model for laser directed energy deposition (powder-fed additive manufacturing): from single-track to multi-track and multi-layer. Opt. Laser Technol. 109, 584–599. https://doi.org/10.1016/J.OPTLASTEC.2018.08.015.

Khairallah, Sa., Anderson, A., 2014. Mesoscopic simulation model of selective laser melting of stainless steel powder. J. Mater. Process. Technol. 214, 2627–2636. https://doi.org/10.1016/j.jmatprotec.2014.06.001.

Knapp, G.L., Mukherjee, T., Zuback, J.S., Wei, H.L., Palmer, T.A., De, A., DebRoy, T., 2017. Building blocks for a digital twin of additive manufacturing. Acta Mater. 135, 390–399. https://doi.org/10.1016/j.actamat.2017.06.039.

Kou, S., 2002. Welding Metallurgy, 2nd ed. cambridge.org.https://doi.org/10.1002/0471434027.

Kurz, W., Fisher, D., 1998. Fundamentals of Solidification, 4th ed. Trans Tech Publications. CRC Press https://doi.org/AR1RAAAAMAAJ.

Kurz, W., Fisher, D.J., 1981. Dendrite growth at the limit of stability: tip radius and spacing. Acta Metall. 29, 11–20. https://doi.org/10.1016/0001-6160(81)90082-1.

Kurz, W., Giovanola, B., Trivedi, R., 1986. Theory of microstructural development during rapid solidification. Acta Met. 34, 823–830. https://doi.org/10.1007/978-94-009-4456-5_24.

Lampa, C., Kaplan, A.F.H., Powell, J., Magnusson, C., 1997. An analytical thermodynamic model of laser welding. J. Phys. D Appl. Phys. 30, 1293–1299. https://doi.org/10.1088/0022-3727/30/9/004.

Lia, F., Park, J.Z., Keist, J.S., Joshi, S., Martukanitz, R.P., 2018. Thermal and micro-structural analysis of laser-based directed energy deposition for Ti-6Al-4V and Inconel 625 deposits. Mater. Sci. Eng. A 717, 1–10. https://doi.org/10.1016/j.msea.2018.01.060.

Liang, Y.-J., Li, A., Cheng, X., Pang, X.-T., Wang, H.-M., 2016. Prediction of primary dendritic arm spacing during laser rapid directional solidification of single-crystal nickel-base superalloys. J. Alloys. Compd. 688, 133–142. https://doi.org/10.1016/J.JALLCOM.2016.06.289.

Liang, Y.J., Cheng, X., Li, J., Wang, H.M., 2017. Microstructural control during laser additive manufacturing of single-crystal nickel-base superalloys: new processing–microstructure maps involving powder feeding. Mater. Des. 130, 197–207. https://doi.org/10.1016/j.matdes.2017.05.066.

Manvatkar, V.D., Gokhale, A.A., Reddy, Jagan, G, Venkataramana, De, A., 2011. Estimation of melt pool dimensions, thermal cycle, and hardness distribution in the laser-engineered net shaping process of austenitic stainless steel. Metall. Mater. Trans. A Phys. Metall. Mater. Sci. 42, 4080–4087. https://doi.org/10.1007/s11661-011-0787-8.

Marchese, G., Garmendia Colera, X., Calignano, F., Lorusso, M., Biamino, S., Minetola, P., Manfredi, D., 2017. Characterization and comparison of inconel 625 processed by selective laser melting and laser metal deposition. Adv. Eng. Mater. 19, 1600635. https://doi.org/10.1002/adem.201600635.

Mazumder, J., Qi, H., 2005. Fabrication of 3-D components by laser aided direct metal deposition. Critical Review: Industrial Lasers and Applications. pp. 38–59. https://doi.org/10.1117/12.601652.

Muvvala, G., Patra Karmakar, D., Nath, A.K., 2017. Online monitoring of thermo-cycles and its correlation with microstructure in laser cladding of nickel based super alloy. Opt. Lasers Eng. 88, 139–152. https://doi.org/10.1016/j.optlaseng.2016.08.005.

Ou, W., Mukherjee, T., Knapp, G.L., Wei, Y., DebRoy, T., 2018. Fusion zone geometries, cooling rates and solidification parameters during wire arc additive manufacturing. Int. J. Heat Mass Transf. 127, 1084–1094. https://doi.org/10.1016/j.ijheatmasstransfer.2018.08.111.

Picasso, M., Marsden, C.F., Wagniere, J.D., Frenk, A., Rappaz, M., 1994. A simple but realistic model for laser cladding. Metall. Mater. Trans. B 25, 281–291. https://doi.org/10.1007/BF02665211.

Pinkerton, A.J., Li, L., 2004. Modelling the geometry of a moving laser melt pool and deposition track via energy and mass balances. J. Phys. D Appl. Phys. 37, 1885–1895. https://doi.org/10.1088/0022-3727/37/14/003.

Roy, S., Juha, M., Shephard, M.S., Maniatty, A.M., 2018. Heat transfer model and finite element formulation for simulation of selective laser melting. Comput. Mech. 62, 273–284. https://doi.org/10.1007/s00466-017-1496-y.

Rubenchik, A.M., King, W.E., Wu, S.S., 2018. Scaling laws for the additive manufacturing. J. Mater. Process. Technol. 257, 234–243. https://doi.org/10.1016/J.JMATPROTEC.2018.02.034.

Sames, W.J.W., List, F.A.F., Pannala, S., Dehoff, R.R.R., Babu, S.S., 2016. The metallurgy and processing science of metal additive manufacturing. Int. Mater. Rev. 61, 315–360. https://doi.org/10.1080/09506608.2015.1116649.

Scipioni Bertoli, U., MacDonald, B.E., Schoenung, J.M., 2019. Stability of cellular microstructure in laser powder bed fusion of 316L stainless steel. Mater. Sci. Eng. A 739, 109–117. https://doi.org/10.1016/J.MSEA.2018.10.051.

Steen, W.W.M., Mazumder, J., 2010. Laser Material Processing. Springer Science & Business Mediahttps://doi.org/10.1016/0924-0136(93)90021-W.

Tan, W., Wen, S., Bailey, N., Shin, Y.C., 2011. Multiscale modeling of transport phenomena and dendritic growth in laser cladding processes. Metall. Mater. Trans. B 42, 1306–1318. https://doi.org/10.1007/s11663-011-9545-y.

Toyserkani, E., Khajepour, A., 2006. A mechatronics approach to laser powder deposition process. Mechatronics 16, 631–641. https://doi.org/10.1016/J.MECHATRONICS.2006.05.002.

Toyserkani, E., Khajepour, A., Corbin, S., 2004a. 3-D finite element modeling of laser cladding by powder injection: effects of laser pulse shaping on the process. Opt. Lasers Eng. 41, 849–867. https://doi.org/10.1016/S0143-8166(03)00063-0.

Toyserkani, E., Khajepour, A., Corbin, S.S., 2004b. Laser Cladding. CRC presshttps://doi.org/10.1201/9781420039177.

Vilar, R., Almeida, A., 2015. Repair and manufacturing of single crystal Ni-based superalloys components by laser powder deposition—a review. J. Laser Appl. 27, S17004. https://doi.org/10.2351/1.4862697.

Wang, Q., Li, J., Gouge, M., Nassar, A.R., Michaleris Pan, P., Reutzel, E.W., 2016. Physics-based multivariable modeling and feedback linearization control of melt-pool geometry and temperature in directed energy deposition. J. Manuf. Sci. Eng. 139, 021013. https://doi.org/10.1115/1.4034304.

Wang, Z., Palmer, T.A., Beese, A.M., 2016. Effect of processing parameters on microstructure and tensile properties of austenitic stainless steel 304L made by directed energy deposition additive manufacturing. Acta Mater. 110, 226–235. https://doi.org/10.1016/j.actamat.2016.03.019.

Wei, H.L., Mazumder, J., DebRoy, T., 2015. Evolution of solidification texture during additive manufacturing. Sci. Rep. 5, 16446. https://doi.org/10.1038/srep16446.

Wen, S., Shin, Y.C., 2010. Modeling of transport phenomena during the coaxial laser direct deposition process. J. Appl. Phys. 108, 044908. https://doi.org/10.1063/1.3474655.

Whitesell, H.S., Li, L., Overfelt, R.A., 2000. Influence of solidification variables on the dendrite arm spacings of Ni-based superalloys. Metall. Mater. Trans. B Process Metall. Mater. Process. Sci. 31, 546–551. https://doi.org/10.1007/s11663-000-0162-4.

Wolff, S.J., Lin, S., Faierson, E.J., Liu, W.K., Wagner, G.J., Cao, J., 2017. A framework to link localized cooling and properties of directed energy deposition (DED)-processed Ti-6Al-4V. Acta Mater. 132, 106–117. https://doi.org/10.1016/j.actamat.2017.04.027.

Xu, X., Mi, G., Chen, L., Xiong, L., Jiang, P., Shao, X., Wang, C., 2017. Research on microstructures and properties of Inconel 625 coatings obtained by laser cladding with wire. J. Alloys. Compd. 715, 362–373. https://doi.org/10.1016/J.JALLCOM.2017.04.252.

Yadroitsev, I., Krakhmalev, P., Yadroitsava, I., Johansson, S., Smurov, I., 2013. Energy input effect on morphology and microstructure of selective laser melting single track from metallic powder. J. Mater. Process. Technol. 213, 606–613. https://doi.org/10.1016/j.jmatprotec.2012.11.014.

Yang, Y., Knol, M.F.F.M., van Keulen, F., Ayas, C., 2018. A semi-analytical thermal modelling approach for selective laser melting. Addit. Manuf. 21, 284–297. https://doi.org/10.1016/j.addma.2018.03.002.

Yin, H., Felicelli, S.D., 2010. Dendrite growth simulation during solidification in the LENS process. Acta Mater. 58, 1455–1465. https://doi.org/10.1016/J.ACTAMAT.2009.10.053.

Zhang, K., Wang, S., Liu, W., Shang, X., 2014. Characterization of stainless steel parts by laser metal deposition shaping. Mater. Des. 55, 104–119. https://doi.org/10.1016/j.matdes.2013.09.006.

Zheng, B., Zhou, Y., Smugeresky, J.E.E., Schoenung, J.M.M., Lavernia, E.J.J., 2008. Thermal behavior and microstructure evolution during laser deposition with laser-engineered net shaping: part II. Experimental investigation and discussion. Metall. Mater. Trans. A Phys. Metall. Mater. Sci. 39, 2237–2245. https://doi.org/10.1007/s11661-008-9566-6.